

**Intercomparison of Fast airborne Ozone Instruments to measure Eddy Covariance Fluxes:
Spatial variability in deposition at the ocean surface and evidence for cloud processing**

Randall Chiu^{1,2}, Florian Obersteiner³, Alessandro Franchin⁴, Teresa Campos⁴, Adriana Bailey⁴,
5 Christopher Webster⁴, Andreas Zahn³, and Rainer Volkamer^{1,2,*}

1 Department of Chemistry, University of Colorado Boulder, 215 UCB, Boulder, CO, USA

2 Cooperative Institute for Research in Environmental Sciences (CIRES), University of Colorado
Boulder, 216 UCB, Boulder, CO, USA

3 Karlsruhe Institute of Technology, Institute of Meteorology and Climate Research (IMK),
10 Dept. ASF, Hermann-von-Helmoltz-Platz 1 D-76344 Eggenstine-Leopoldshafen, Germany

4 National Center for Atmospheric Research, P.O. Box 3000, Boulder, CO, 80307, USA

* corresponding authors: randall.chiu@colorado.edu, rainer.volkamer@colorado.edu

Abstract

15 The air-sea exchange of ozone (O₃) is controlled by chemistry involving halogens, dissolved
organic carbon and sulfur in the sea surface microlayer. Calculations also indicate faster ozone
photolysis at aqueous surfaces, but the role of clouds as ozone sink is currently not well
established. Fast response ozone sensors offer opportunities to measure eddy covariance (EC)
ozone fluxes in the marine boundary layer. However, intercomparisons of fast airborne O₃
20 sensors, and EC O₃ fluxes measured on aircraft have not been conducted before. In April 2022,

the Technical Innovation Into Iodine and GV aircraft Environmental Research (TI³GER) field campaign deployed three fast ozone sensors (gas chemiluminescence and a combination of UV absorption with coumarin chemiluminescence detection, CID) together with a fast water vapor sensor and anemometer to study iodine chemistry in the troposphere and stratosphere over

25 Colorado and over the Pacific Ocean near Hawaii and Alaska. Here, we present an instrument comparison between the NCAR Fast O₃ instrument (FO₃, gas-phase CID) and two KIT Fast AIRborne Ozone instruments (FAIRO, UV absorption and coumarin CID). The sensors have comparable precision $<0.4\% \text{ Hz}^{-0.5}$ ($0.15 \text{ ppbv Hz}^{-0.5}$), and ozone volume mixing ratios (vmr) generally agreed within 2% over a wide range of environmental conditions: $10 < \text{O}_3 < 1000$

30 ppbv; below detection $< \text{NO}_x < 7 \text{ ppbv}$; and $2 \text{ ppmv} < \text{H}_2\text{O} < 4\% \text{ VMR}$. Both instrument designs are demonstrated to be suitable for EC flux measurements and were able to detect O₃ fluxes with exchange velocities (defined as positive for upward) as slow as $-0.010 \pm 0.004 \text{ cm s}^{-1}$, which is in the lower range of previously reported measurements. Additionally, we present two case studies. In one, the direction of ozone and water vapor fluxes were reversed ($v_{\text{O}_3} = +0.134 \pm 0.005 \text{ cm s}^{-1}$), suggesting that overhead evaporating clouds could be a strong ozone sink. Further work is

35 needed to better understand the role of clouds as a possibly widespread sink of ozone in the remote marine boundary layer. In the second case study, v_{O_3} are negative (varying by a factor of 6-10 from -0.036 ± 0.006 to $-0.003 \pm 0.004 \text{ cm s}^{-1}$), while the water vapor fluxes are consistently positive due to evaporation from the ocean surface and spatially homogeneous. This case study

40 demonstrates that the processes governing ozone and water vapor fluxes can become decoupled and illustrates the need to elucidate possible drivers (physical, chemical, or biological) of the variability in ozone exchange velocities on fine spatial scales ($\sim 20 \text{ km}$) over remote oceans.

1. Introduction

45 In the troposphere, ozone is a pollutant with adverse health effects for both animals and plants. Eddy covariance (EC) is a technique that has been commonly employed to determine the fluxes of ozone to terrestrial and marine ecosystems. In terrestrial environments, EC flux measurements have been made over periods of months to years (Bauer et al., 2000; Güsten and Heinrich, 1996). Over land, uptake to soils and plant stomata are the major sink of ozone (Clifton et al., 2020; 50 Massman et al., 1995). Consequently, previous campaigns have measured ozone fluxes over a variety of terrestrial settings including agricultural lands (Lamaud et al., 2009; Massman et al., 1995; Stella et al., 2011; Zhu et al., 2015, 2020, 2014), forests (Altimir et al., 2006; Fares et al., 2014; Finco et al., 2017; Juráň et al., 2019; Kammer et al., 2019; Lamaud et al., 2002; Rannik et al., 2012; Vermeuel et al., 2021; Zeller, 2002; Zeller and Nikolov, 2000), grasslands (Muller et al., 2009; Wohlfahrt et al., 2009), peatlands (El-Madany et al., 2017), and deserts (Güsten et al., 55 1996).

Oceans account for $\sim 1/3$ of global ozone dry deposition (Ganzeveld et al., 2009). Ozone losses in the marine environment may be driven by reactions with halogens such as iodide (Saiz-Lopez et al., 2012) or with double bonds from fatty acid precursors (Chiu et al., 2017). EC flux 60 measurements of ozone have also been performed in coastal and oceanic settings (Bariteau et al., 2010; Gallagher et al., 2001; Helmig et al., 2006) and over sea ice (Barten et al., 2023; Muller et al., 2012).

Whereas EC flux measurements of ozone are numerous, comparison studies are fewer. Ozone fluxes from EC methods have been compared to those from gradient measurements (Loubet et al., 2013; Muller et al., 2009; Zhu et al., 2020) and dynamic chamber methods (Plake et al., 65

2015). Over grassland, Plake et al., (2015) report that dynamic chamber methods agree “well” with EC flux methods (within 11-26%). Over maize fields, Zhu et al., (2020) describe the discrepancy between EC flux and gradient methods as “not very good,” with gradient methods measuring ozone fluxes 11.7 – 45.6% higher than those measured by EC flux methods.

70 Furthermore, comparisons of co-located EC flux measurements are uncommon, and complicated due to vertical gradients in the measured fluxes that may explain differences of 10% between measurements on towers (measured by chemiluminescence) and aircraft (measured by a TECO-49) (Massman et al., 1995). To our knowledge, the only aircraft instrument intercomparison for ozone EC flux was performed by Muller et al., (2010), who compared two identical dry
75 chemiluminescence instrumental clones over grassland and found differences up to 12% due to differing sensitivities of chemiluminescent discs. Furthermore, a water sensitivity for chemiluminescent measurement techniques (Ridley et al., 1992) has been suggested to propagate onto EC ozone flux measurements (Boylan et al., 2014), and methods for water correction differ between different methods for measuring ozone. More commonly, a fast ozone instrument is
80 compared to other ozone instruments only in terms of concentrations (Conley et al., 2011; Hannun et al., 2020). There is currently no intercomparison of different fast ozone instruments that rely on different measurement concepts and respond differently to water sensitivities on research aircraft. Furthermore, the error analysis to estimate EC flux uncertainties is not well developed and is not always treated consistently. This leaves room for instrument and method
85 uncertainty as drivers for overall uncertainty in parameterizing ozone exchange velocities and deposition. Here we eliminate spatial gradients as a source of uncertainty in ozone EC flux intercomparisons by deploying three ozone instruments of two different designs on the same research aircraft in remote marine air. We further use the agreement found among the three

sensors to evaluate and refine the EC flux error analysis and define better criteria of use to
90 estimate detection limits.

(Massman et al., 1995)Muller et al., (2010)(Conley et al., 2011)Hannun et al., (2020)

Section 2 introduces the Technological Innovation Into Iodine and GV Environmental Research
(TI³GER) field campaign and describes the instruments and methods used to calculate fluxes of
O₃ and H₂O by the EC technique. Section 3 compares the O₃ concentrations and EC fluxes in
95 context with the available literature over oceans and assesses spatial variability and the EC flux
error budget. Finally, Section 4 summarizes the conclusions and gives an outlook for future
work.

2. Methods

2.1. The TI³GER field campaign

100 In April 2022, the Technological Innovation Into Iodine and GV Environmental Research
(TI³GER) technical campaign was performed to lay the groundwork for future field
investigations into the interactions of ozone and iodine in the upper troposphere lower
stratosphere (UTLS). In total, eight research flights (RFs) were conducted, with RFs 01 and 02
over the continental United States, and RFs 03-08 conducted over the Pacific Ocean near Hawaii
105 and Alaska. Among the instruments flown on TI³GER were three ozone instruments, two of
which were of an identical design. The NCAR Fast O₃ instrument operates by NO₂
chemiluminescence and has been in use since the early 1970s (Pearson, R. and Stedman, 1980;
Ridley et al., 1972, 1992; Ridley and Howlett, 1974). Two copies of the Fast AIRborne Ozone
(FAIRO) instrument from KIT were also deployed (FAIRO 1 and FAIRO 2). The FAIRO

110 instruments operate by coumarin chemiluminescence calibrated against a dual-beam UV
absorption photometer.

One objective of TI³GER was to compare the performance of the two instrument designs and
evaluate their ability to measure EC flux of ozone on the NCAR/NSF Gulfstream 5 (GV)
platform. The GV measures 3-D winds using a combination of measurements from pitot, static,
115 and radome sensors; the vertical components of these 3-D winds are needed for EC analysis. In
all, EC flux measurements were performed during nineteen legs flown over the Pacific Ocean.
The continental flights are not discussed here because they did not include many EC flux
measurements. A table of the relevant meteorological and ocean-state variables appears in the
supplement as Table S1. Figure 1 shows a map of where attempts were made to measure EC flux.
120 The arrows point to the locations of the flux legs with curves showing the five-day back-
trajectories of the sampled air calculated by HYSPLIT (Rolph et al., 2017; Stein et al., 2015)
using the National Oceanographic and Atmospheric Administration (NOAA) National Centers
for Environmental Prediction (NCEP) Global Forecasting System (GFS) meteorological dataset.
Flux legs were typically 5-10 minutes long. At airspeeds of $\sim 110 \text{ m s}^{-1}$, flux legs covered 30-70
125 km. A typical flight module consisted of three legs flown in a stacked manner (RF03-B, RF03-C,
and RF07-A). However, in the case of RF03-B, fluxes were below detection. Hence, other flight
legs were opportunistically used for flux calculations on level legs in the marine boundary layer
(MBL). Dedicated flux segments were accompanied by profile descents and ascents.

130 2.2. Ozone Instrumentation

Three ozone instruments were installed on the GV. Two (the FAIRO instruments) were of an identical design.

2.2.1. The NCAR Fast O3 instrument

The NCAR Fast O3 instrument sampled from a HIAPER Modular Inlet (HIMIL). All tubing was
135 made of Teflon. The total mass flow in the inlet was 2370 sccm. The sample line was 70 cm long with an inner diameter of 6.4 mm. From this flow, Fast O3 sampled 500 sccm through a 140 cm-long line with an inner diameter of 3.8 mm at a constant absolute pressure of 70 torr. Total residence time is 0.75 s. Fast O3 provides 10 Hz data by detecting photons from the following chemiluminescence reaction:



The excited NO₂ in R2 can also be quenched by collision with other molecules. Water vapor quenches excited NO₂ more efficiently than do nitrogen or oxygen (Matthews et al., 1977), so after time stamp synchronization among the instruments (see Sect. 2.3.), the following water
145 vapor correction is applied (Ridley et al., 1992):

$$[O_3]_{corrected} = [O_3] \times (1 + 4.3(\pm 0.3) \times 10^{-3} \times [H_2O]) \quad (1)$$

where [O₃] is the ozone mixing ratio in ppbv, and [H₂O] is the water vapor mixing ratio in permille by volume of dry air.

The water vapor correction is performed using VCSEL water vapor data (see Sect. 2.2.) that are
150 collected at a higher frequency (25 Hz) than are the Fast O3 data. Thus, the water vapor

correction is expected to contribute negligible bias to the EC flux calculations. To assess the potential impact of the water vapor correction on Fast O3 EC fluxes, the constant in eq. (1) was varied from its minimum and maximum estimated values (4.0 – 4.6) in the RF03-C-2 leg; the change in this parameter resulted in biases in the EC flux results of no more than 0.7%.

155 Neglecting the water vapor correction altogether decreased the calculated exchange velocity (see Sect. 2.4) by 5% from 0.131 cm s^{-1} to 0.124 cm s^{-1} (see Table 2). Using the average water vapor concentration during the entire leg for the water vapor correction increases the calculated exchange velocity 2% to 0.134 cm s^{-1} ; this case represents the extreme case in which water vapor reaching the ozone instruments is completely smeared out by longitudinal diffusion. We
160 conclude that water vapor interference in the Fast O3 instrument contributes at most 5% to the ozone flux uncertainty, and likely less than 2%. The 0.131 cm s^{-1} value is in good agreement with the EC flux results from FAIRO 1 and FAIRO 2, and the Fast O3 exchange velocities are not systematically higher or lower than those from FAIRO 1 or FAIRO 2. The water vapor interference for the coumarin instruments goes in the opposite direction than for the UV
165 instruments, i.e. water vapor makes Fast O3 less sensitive to ozone, but FAIRO more sensitive (Güsten et al., 1992; Schurath et al., 1991; Zahn et al., 2012). The fact that all three instruments agree after water vapor correction gives us confidence that water vapor bias is removed. The Fast O3 instrument was calibrated after the campaign using a TECO Model 49i-PS ozone primary standard. The typical instrument detection limit is $0.5 \text{ ppbv Hz}^{-0.5}$ with an accuracy not better
170 than 5% at high signal to noise.

2.2.2. The KIT Fast AIRborne Ozone (FAIRO) instruments

Two identical FAIRO instruments were deployed. The FAIRO instruments were independently checked for proper functioning both prior to the campaign using an Ansyco (now Gasmot

Technologies) SYCOS KT-O3M and after the campaign using a TECO 49i-PS. The FAIROs
175 sampled from a separate HIMIL (aft-facing inlet line) through a PFA line with a length of 4.3 m
and a 0.42 cm (1/6 in.) inner diameter. Outside air was pulled at 11 vol.-L min⁻¹ at ambient
pressure by a Vacuubrand MD1 pump downstream of the instruments. Residence time in the line
is approximately 0.3 s. The flow was split at a T-fitting ~0.5 m ahead of the FAIROs. Internally,
2.5 vol.-L min⁻¹ of flow went to the UV photometer, which measured ozone absorption around
180 255 nm within the Hartley band. The O₃ absorption cross section and temperature dependence
are taken from (Barnes and Mauersberger, (1987). The UV absorption channel operates at 0.25
Hz. A second, faster 12.5 Hz coumarin chemiluminescence detector (CID) (Ermel et al., 2013) is
calibrated against the UV channel and provides the data used in EC flux calculations. The dual
detector FAIRO design has two main advantages over the Fast O₃ instrument: the FAIROs are
185 lightweight (approx. 14 kg, 19” rack slot with 3 height units per instrument) and do not require
operating fluids such as compressed gases. Scattering by aerosols and absorption by aromatic
compounds and water vapor are well-known interferences for UV ozone instruments (Dunlea et
al., 2006). The potential for humidity changes to interfere with FAIRO UV photometers was
further investigated and is found to be small yet not fully insignificant (see Supplementary
190 Figure S1). Interference from aerosols is avoided by the backward-facing sample inlet and
aromatic compounds are expected to be minimal in the pristine air sampled in RFs 03-07. A
detailed technical description of FAIRO CID can be found in (Zahn et al., (2012). The instrument
detection limit is below 1 ppbv Hz^{-0.5} (provided by the CID) and the total uncertainty 1.5%
(mainly determined by the uncertainty of the O₃ absorption cross section found in the literature)
195 or 1.5 ppbv, whatever is lower.

2.2. Water vapor: VCSEL

Water vapor in the free stream above the GV is measured by the vertical cavity surface emitting laser (VCSEL) hygrometer. VCSEL is an open-path optical cavity measuring two absorption lines for high dynamic range: a strong line at 1854.03 nm for low vmrs and a weak line at 1853.37 nm for high vmrs. Data are collected at 25 Hz. During the flux legs, water vapor is always above the VCSEL detection limit of 0.8 ppmv. Details about the operation of VCSEL can be found in Zondlo et al., (2010).

2.3. Instrument time stamp synchronization

The three ozone instruments and the GV variables are measured on four independent time stamps, each with its own potential offset and drift. Conveniently, ozone and water vapor vmrs are occasionally anticorrelated (and less frequently, correlated). We use these anticorrelation events to synchronize each ozone instrument with VCSEL since VCSEL is already synchronized to the anemometer. First, the ozone and VCSEL signals are interpolated to a common 100 Hz timestamp. Second, each ozone time series is visually inspected to identify unambiguous anticorrelation events with the water vapor time series in the periods before and after each flux leg. Third, the time lag at each anticorrelation event is determined by shifting the interpolated ozone signal until the absolute value of the covariance between the ozone and VCSEL signals is maximized. Finally, with the time lag identified both before and after the leg, the ozone time stamp is linearly stretched to match the VCSEL time stamp. Anticorrelation events are not uncommon. For instrument intercomparison, anticorrelation events from the start and end of the entire flight are used to synchronize data; averaging the synchronized data over 10 s is sufficient to resolve any residual (<100 ms) synchronization uncertainty. For flux sampling, anticorrelation events were found before and after each flux leg.

2.4. Eddy covariance flux calculations

220 Eddy covariance (EC) is a commonly used technique to determine the fluxes of gases in well-mixed surface layers. Given chemical concentration and wind speed data, EC flux can be calculated as:

$$ECflux = cov(x, w) = \frac{1}{n} \sum_{i=1}^n (x_i - \bar{x}) (w_i - \bar{w}) \quad (2)$$

where x is the concentration of the chemical species and w is the vertical wind component. For
225 non-stationary conditions, wavelet analysis (WA) is commonly employed instead (Torrence and Compo, 1998). Stationarity is not required for WA because WA decomposes the total flux into component fluxes at different frequencies. In WA, the time series are first transformed into a wavelet by convolution with a wavelet function:

$$W_s(a, b) = \int_{-\infty}^{\infty} s(t) \psi_{a,b}(t) dt \quad (3)$$

230 $\psi_{a,b}(t) = \frac{1}{\sqrt{a}} \psi_0\left(\frac{t-b}{a}\right)$ (4)

where a and b are scale and translation factors for Ψ_0 , the “mother wavelet” function. For eddy covariance applications, the typical choice for the mother wavelet is the Morlet wavelet:

$$\psi_0(\eta) = \pi^{-\frac{1}{4}} e^{i\omega_0\eta} e^{-\frac{\eta^2}{2}}, \omega_0 = 6 \quad (5)$$

The WA flux is then calculated as $|W_w W_x|$, where W_w and W_x are the wavelet coefficients of
235 wind and ozone, respectively (Wolfe et al., 2018).

A challenge in EC flux error analysis is that EC flux is not a measurement from a single instrument, but rather the combination of measurements from two instruments: a chemical

monitor of some sort and an anemometer. For individual instruments, estimation of the limit of detection (LOD) from random error (RE) can be straightforward:

$$240 \quad LOD = \alpha \times RE \quad (6)$$

where α is a dimensionless factor corresponding to the confidence level (1.96 for 95% CL, 3 for 99% CL). The standard deviation of blank measurements can be used to estimate the RE of a single instrument. However, this method is not applicable to flux measurements due to the lack of true “blanks” matching the chemical and meteorological conditions of interest.

245 Several methods for determining the LOD of EC flux measurements have been put forth based on statistical treatments of the cross-covariance of the chemical and wind data at different time lags. For example, (Langford et al., (2015) present the following formula for estimating the root mean squared error (RE_{RMSE}):

$$RE_{RMSE} = \sqrt{0.5 \left(\left(\sigma_{f_{w'c'}[-\Gamma]} \right)^2 + \left(\overline{f_{w'c'}[-\Gamma]} \right)^2 + \left(\sigma_{f_{w'c'}[+\Gamma]} \right)^2 + \left(\overline{f_{w'c'}[+\Gamma]} \right)^2 \right)} \quad (7)$$

250 where $\sigma_{f_{w'c'}}$ and $\overline{f_{w'c'}}$ are the standard deviation and average of the cross-covariance, and $\pm\Gamma$ represent time lags far away from the true time lag between the wind and chemical measurements. Currently, no well-established method for estimating the LOD of EC and WA fluxes is commonly accepted. The number of independent replicate measurements of ozone available during TI³GER gave us the unique opportunity to explore, evaluate and optimize
255 methods to constrain the uncertainty of EC fluxes, since the standard deviation of the fluxes measured between the individual instruments can give a sense of the magnitude of the “true” error.

A MATLAB toolkit (AirChem/FluxToolbox: Collections of scripts for eddy covariance flux calculations (both traditional and wavelet-based)., 2023) was used for this work. Raw data must
260 be pre-processed to remove data gaps before inputting to the toolbox. Data gaps are removed by linear interpolation; such gaps are rare, and interpolation is used only to remove up to three or four points (out of ~2000-4000 which is typical for a flux leg). Because the GV data are recorded at higher resolution than are the ozone data, the wind and VCSEL data are binned to each ozone instrument's corrected time stamp.

265 For EC fluxes, the toolbox detrends the data with a boxcar method in a user-defined time frame. The lengths of the detrending time frames were selected to balance being short enough to remove systematic cross-covariance structures with being long enough to retain low-frequency fluxes. A detrending time of 10 s was used in all fluxes presented below. For all flux legs, various detrending times were tested to see whether visually identifiable structures could be observed in
270 the cross-covariance. A uniform 10 s detrending time was found to remove systematic structures from all flux legs. To minimize the number of subjective inputs, we did not attempt to customize the detrending time for each flux leg. Because detrending accounts for meteorological conditions rather than instrument response, meaningful intercomparisons could be performed using uniform conditions and consistent detrending times. At typical aircraft speeds, 10 s corresponds to 1-1.2
275 km. In addition to calculating an eddy covariance flux, the toolbox also calculates WA flux (Torrence and Compo, 1998) and outputs cospectra as a function of frequency.

In contrast to common practice, we express ozone fluxes in terms of exchange velocity (v_e) rather than deposition velocity (v_d), where:

$$v_e = \frac{flux(ppbms^{-1})}{concentration(ppb)} \times \frac{100cm}{1m} \quad (8)$$

280 Exchange velocity is the same as deposition velocity apart from the lack of a negative sign, i.e. upward directed fluxes have positive v_e . We use v_e rather than v_d because some interesting case studies presented have upward directed fluxes, which are more intuitively represented using positive signs.

Notably, fluxes and cross-covariances in principle have the same units ($\text{molec cm}^{-2} \text{s}^{-1}$ or ppb m
285 s^{-1}). However, we use "covariance" to refer to the cross-covariance calculated for different lag times by our code, and "flux" to identify an atmospheric state. This distinction is useful when discussing EC flux errors, which are estimated from cross-covariances at time lags departing from the true lag between instruments. Whereas such cross-covariances represent true statistical covariance, they do not represent atmospheric fluxes.

290 3. Results and Discussion

3.1. Instrument intercomparison

Figure 2 shows the time series of O₃ from all three sensors from RF03 as an example. Panel A shows the altitude of the GV, and Panel B shows the water vapor and ozone time series for the entire flight. Water vapor/ozone time synchronization was performed as close to the beginning and the end of the flight as correlation events could be visually identified; close-ups of these 295 events are shown in Panels C and E. For EC flux legs, time synchronization was performed before and after each leg rather than for the entire flight. Because the Fast O₃ instrument computer was not synchronized with the time server, there was an artificial delay of 5 s between it and VCSEL. After the time synchronization procedure, even artificial clock delays are resolved 300 to within ± 0.1 s. However, Panel D shows that the ozone signals are not synchronized with each other or to a water vapor correlation event midway through the flight. The discrepancy could be caused by a combination of different flow conditions at different altitudes or instrumental clock drift. However, because the FAIRO instruments share an inlet line that forks only in the last ~ 0.5 m, inlet line flow differences alone cannot explain their time offset. Inspection of the delays from 305 each RF show that the ozone clocks drift no more than ± 0.7 s (typically ≤ 0.5 s). For ozone instrument comparisons, data were averaged over 10 s to prevent bias from synchronization errors.

Aggregated data from RF03-07 are shown in Figure 3, Panel A. Ozone vmrs measured by each FAIRO are plotted against ozone vmrs measured by Fast O₃. Linear fits of the FAIRO vmrs are 310 also shown. The data from both instrument designs appear to be linear, with a 2% overall difference. In Panels B-D, the absolute and relative differences between each instrument and the

average of all three instruments are shown. In all cases, data are color-coded for high water vapor (concentration $> 1.4 \times 10^{17}$ molec cm⁻³, blue) and high NO_x (volume mixing ratio > 200 pptv, red). GPS altitude, VCSEL water vapor concentration, and NO_x are also shown in the

315 background of Panels B, C, and D, respectively, for context. Neither the absolute nor the relative differences from the average exhibit systematic behavior depending on water vapor or NO_x. The effect of humidity changes did not reveal any obvious explanation for O₃ differences when comparing individual instruments to the instrument mean (not shown). For the effect of changing humidity when comparing FAIRO instruments, see Supplementary Figure S1; for the effect of

320 changing humidity on FAIRO to Fast O₃ comparison, see Supplementary Figure S2. Although the persistent differences from average are accompanied by high NO_x conditions between ~00:00-02:00 on 21 April 2022 UTC, high NO_x conditions between ~19:30-20:00 on 20 April 2022 UTC are not accompanied by similar differences. High water vapor during a low-altitude flux leg at 21:00 UTC is accompanied by agreement amongst all three instruments within 2%.

325 The agreement of the instruments was also evaluated individually for RFs 03-07. The fit results for each flight are shown in Table 1.

A subset of flux legs with low ozone variability was used to infer an upper limit of the precision of each instrument, as the contribution by additional atmospheric variability cannot be fully eliminated. The ozone time series from each flux leg is smoothed over one second and the range

330 is calculated of the smoothed data. Variability is calculated as the relative range of ozone in that leg. Flux legs are characterized as low-variability if the relative range of the smoothed time series is less than 5% for at least two instruments. Precision is calculated as the standard deviation of the unsmoothed time series. All three instruments have comparable precision, with

Fast O3 precision at 1.4% (0.45 ppb) at 10 Hz, FAIRO 1 at 1.2% (0.36 ppb) at 12.5 Hz, and
335 FAIRO 2 at 1.1% (0.36 ppb) at 12.5 Hz. These precision estimates represent an upper bound as
some of the variability could be true atmospheric variability. More detail on the precision
calculations can be found in Table S2 of the supplement.

3.2. Eddy covariance flux

Potential temperature (Θ) and equivalent potential temperature (Θ_e) profiles are used to
340 determine whether flux legs were conducted within the MBL. Example profiles are shown in
Figure 4. The profiles shown are taken from both descent and ascent except in the case of the
RF03-C flux legs, which were performed as the plane approached the airport for landing. The
flux legs in RF04 were conducted over the tropical Pacific Ocean, and both profiles indicate an
MBL height of ~ 800 m. The utility of Θ_e in determining the MBL height is evident in the RF06-
345 A legs, which were conducted off the coast of Alaska. The Θ profile on the descent does not
unambiguously show an MBL height, but the Θ_e profile clearly indicates an MBL height of ~ 200
m on both the descent and ascent. Such a shallow MBL near the Kenai Fjords combined with the
strong temperature inversion suggests RF06-A may be subject to distinct "pools" of air; yet the
 Θ_e profiles suggest mixing to the surface. The MBL height in RF03-A is difficult to distinguish
350 and may be ~ 500 m. In all cases, flux legs were conducted at heights well within the MBL except
in RF03, where flux legs were conducted at 107, 476, and 889 m.

Whereas the Fast O3 instrument used constant mass flow at constant pressure, the FAIRO
instruments used constant volume flow at ambient pressure. In principle, the flow rates in the
two instrument designs could differ between the high altitude/low pressure legs typically used
355 for time synchronization and the low altitude/high pressure legs used for flux measurements.

Although the different flow rates can create time lag between wind and ozone data, no systematic error is introduced to the ozone flux because we empirically determine the time offset, and do not prescribe a constant offset in the MATLAB flux toolkit. Rather, the time synchronization is used in conjunction with water vapor fluxes calculated from VCSEL data to find the true ozone time
360 offset.

The time delay between VCSEL and the wind data is determined by calculating the water vapor flux. VCSEL and wind speed data are well-synchronized; in most (12) cases, the water vapor cross-covariance had a peak at a time lag of zero points; in six cases the optimal lag was -1 point on the 12.5 Hz FAIRO time stamp (within 0.08 s). In one case (RF07-A-4) the VCSEL cross-
365 covariance peaked at +5 points, but this is likely a spurious correlation because the VCSEL data from the previous leg was well-synchronized (zero time lag). Cross-covariance and cospectra for ozone and water vapor are shown for selected flux legs (RF03-C-2, RF04-A-1, and RF06-A-1) in Figure 5 (see Sect. 3.4).

Because water vapor fluxes are strong and always above detection, the VCSEL/wind time offset
370 allows us to anchor the ozone time offset and limit our search for an ozone covariance peak to ± 0.7 s from the VCSEL time offset since that is the maximum observed ozone/VCSEL time delay. An ozone flux is reported for an instrument only if a cross-covariance peak is found within that window. A flux is not reported for an instrument if the covariance behavior within that window is primarily one of sign-change, e.g. if the covariance linearly increases from negative to
375 positive, or if there are many zero-crossings. If all three instruments show a covariance that survives this filter, then an average flux is reported for that leg. Of the 19 flux legs, 11 had fluxes that met this criterion, and are summarized in Table 2. A full version of Table 2 with

meteorological conditions and other compounds of interest is included in the Supplementary Information. The cospectra in Fig. 5 peak from 0.1-0.2 Hz, indicating that the bulk of the fluxes occur at 5-10 s time scales. These timescales are typical for fluxes in the MBL, and an order of magnitude larger than the mixing time for the Fast O3 instrument, which for background characterization purposes had zero-air injected from the aircraft inlet. The e-fold rise time was <0.5 s, fast enough not to introduce bias to the flux measurements (see Figure S3 in the SI). Indeed, the cumulative frequency graph (ogive) shows that in the case of RF03-C-2, less than 10% of the total flux is carried on <1 s timescales. Ogives are shown in Figure S4. The residence time in the fast ozone instrument detection volume implied a maximum frequency response of 9 Hz. However, high pass attenuation in the inlet manifold limited the frequency response of the fast O3 instrument to 3 Hz (Lenschow and Raupach, 1991). The FAIRO instruments were not equipped with zero-air injection at the inlet. However, the residence time in the FAIRO flow is shorter than that in Fast O3. A calculation of FAIRO inlet manifold indicates attenuation of high frequency signals above 20 Hz, and therefore was not the limiting factor in the FAIRO instrument frequency response. Thus, the FAIRO was more sensitive to high-frequency fluxes than the Fast O3 instrument.

3.3. Comparison with literature

A previous study has compared ozone EC flux measurements from dry chemiluminescence ozone instruments over grassland (Muller et al., 2010), but to our knowledge no instrument intercomparisons have been performed on board aircraft. Aircraft measurements of ozone flux have been reported before over land (Lenschow et al., 1980; Wolfe et al., 2015, 2018) and over

400 the ocean during PASE (Conley et al., 2011). In the latter, ozone exchange velocities were
-0.024 ± 0.014 cm s⁻¹. Larger data sets for marine ozone flux have been produced by ship
campaigns. The TexAQS cruise reported ozone exchange velocities as large as -0.81 ± 0.27
cm s⁻¹ in coastal channels and -0.034 ± 0.003 cm s⁻¹ in offshore areas, and the STRATUS cruise
measured -0.009 ± 0.001 cm s⁻¹ over open ocean areas (Bariteau et al., 2010; Helmig et al.,
405 2006). All three instruments tested here can detect exchange velocities in the lower range
observed in the remote ocean.

3.4. Constraining the error estimate

Figure 5 shows three examples of covariance plots from flux legs that are representative of the
range of conditions observed. Ozone plots are shown on the left, and the corresponding plots for
410 VCSEL are shown on the right. For all cross-covariances, the Langford LOD is calculated by
using $\Gamma = 30$ s at the beginning and end of the cross-covariance plot, and the Langford 99% CL
LOD for Fast O3 is shown as a light gray shading. Panel A (RF03-C-2) is a case in which all
three ozone instruments measured an upward directed flux and VCSEL (Panel F) shows water
vapor directed downward toward the ocean; this case is described in more detail below. Panel B
415 (RF04-A-1) shows ozone depositing into the ocean and water vapor evaporating out of the
ocean. These two cases are examples of EC flux strong enough to be unambiguously identified
by all three ozone instruments, i.e. that each instrument's flux measurement is above the LOD as
defined by Langford et al. (2015).

Panel C (RF06-A-1) shows a case in which no ozone instrument derived flux is above the
420 Langford LOD. Viewed in isolation, no instrument's cross-covariance is convincing on its own.
However, a small candidate peak can be identified within the ±0.5 s interval.

The average exchange velocity measured by all three instruments in RF06-A-1 is -0.010 cm s^{-1} with a standard deviation of 0.004 cm s^{-1} . The Langford RE_{RMSE} for this leg corresponds to $0.0057\text{-}0.0074 \text{ cm s}^{-1}$ depending on the instrument and thus overstates the error and LOD. We
425 propose a modification of the Langford approach by restricting the interval Γ by calculating the integral time scale. The integral time scale τ characterizes the period over which covariance persists. We estimate τ by integrating outward from the peak until the integral crosses zero (Lenschow et al., 2000). It is possible in certain cases for the calculation of τ to fail. This happened for the VCSEL data shown in Panel H (RF06-A-1). In this case τ was estimated as the
430 width between the second zero-crossings from the peak.

We then apply the Langford RE_{RMSE} calculation to intervals $+\Gamma$ and $-\Gamma$ which are τ in length and are centered around relatively smooth areas of cross-correlation near the candidate peak.

Identifying “smooth” areas was necessarily subjective as the cross-correlation behavior is unique to each leg. The 99% LOD calculated in this modified approach is shown in Figure 5 as dark
435 gray shading. The RE_{RMSE} estimated by the modified approach corresponds to $0.0053\text{-}0.0064 \text{ cm s}^{-1}$, which is more in line with the “true” random error among the three measurements.

3.5. Spatial variability of ozone and water vapor fluxes

The fluxes of ozone and water vapor were in the counterintuitive directions during the RF03-C legs. Figure 6 shows profiles, fluxes, and flight movie stills from this leg. Water vapor was
440 carried downwards, although the ocean surface is usually a water vapor source by evaporation. Conversely, ozone was carried upwards, even though the ocean surface is expected to be an ozone sink. The ozone exchange velocity in this leg (RF03-C-2) was $+0.134 \text{ cm s}^{-1}$ measured at an altitude of 889 m. At a lower altitude of 476 m, (RF03-C-3), the exchange velocity was

+0.097 cm s⁻¹. These velocities are consistent with the lower range of nocturnal entrainment
445 velocities (0.12 – 0.72 cm s⁻¹) measured during the DYCOMS-II campaign over the Eastern
Pacific Ocean (Faloona et al., 2005).

The entrainment velocity as defined by (Deardorff, (1976) is modified here, as in exchange
velocity, such that upward is positive:

$$w_e = \frac{flux(ppbms^{-1})}{\Delta-concentration(ppb)} \times \frac{100cm}{1m} \quad (9)$$

450 In Equation 9, Δ -concentration is the difference in the concentration of a species across a
boundary to the mixed layer. In previous work, the flux at the transition layer (TL) was
extrapolated from the measured fluxes in stacked legs within the MBL and used to estimate the
entrainment velocity (Faloona et al., 2005; Wolfe et al., 2015). This method is not applicable to
the RF03-C legs because the conditions are not mixed to the surface, and because RF03-C-2 is
455 flown en route to the airport in a decoupled TL characterized by minimum O₃ concentrations and
a partial cloud layer near the top (visually estimated from flight videos as ~1 km). The MBL
below extends to ~500m, and the entrainment velocity measured during RF03-C-3 at this altitude
(Figure 6, Panel A, shaded) is 6.3 times smaller than the exchange velocity based on the
observed Δ O₃ of 5.2 ppb and Eq. (9) (existence of a concentration change is not necessarily
460 indicative of a flux); the lower O₃ in the decoupled TL is hence curious. Contributions due to
entrainment of ozone from the free troposphere would result in a negative exchange velocity
during RF03-C-2 (the O₃ profile increases with altitude in the free troposphere) and cannot
explain the positive O₃ exchange velocity observed. If there were a significant O₃ entrainment
from aloft, the observed positive O₃ exchange velocity would be a lower limit.

465 Furthermore, the temporal correlation between the O₃ and H₂O fluxes along RF03-C-2 are
neither consistent with entrainment from above, nor detrainment from below as a driver of the
observed exchange velocities, since the H₂O profile is continuously decreasing with altitude. The
negative H₂O flux during RF03-C-2 cannot be explained by entrainment from above or from
below. Overhead cloud cover can be qualitatively estimated from NO₂ photolysis frequency
470 (J_{NO2}) measured by the HIAPER Airborne Radiation Package (HARP) actinic flux instrument
(Figure 6, Panel B). During cloud-free portions of RF03-C-2 the exchange velocity approaches
zero for both H₂O and O₃, indicating that the observed exchange velocities are cloud related.
There are only two possible explanations: (1) the cloud induces dynamical change to increase O₃
entrainment from the MBL into the decoupled TL (in which case the H₂O source above the
475 aircraft is a lower limit); or (2) the cloud above is a sink of O₃ and a source of H₂O (evaporating
cloud). Notably, the WA time series in Fig. 6 reveals a pronounced maximum O₃ exchange
velocity of +1.8 cm s⁻¹ at the edge of a cloud. Such a large O₃ exchange velocity would require a
five-fold larger ΔO₃ towards the MBL than is compatible with the observed O₃ profile, and
would require O₃ concentrations in the MBL well in excess of 50 ppbv. No such elevated O₃
480 concentrations were observed anywhere near this case study, nor during landing (the O₃
concentration two minutes before landing was 32 ppbv, compatible with the profile shown in Fig.
6). Detrainment of O₃ from below, and entrainment of O₃ from the free troposphere hence cannot
explain the observed positive O₃ exchange velocity during portions of RF03-C-2. We conclude
that a chemical O₃ sink related to an evaporating cloud is the most likely explanation for our
485 observations.

Previously, it was proposed that an increase in aqueous phase chemistry in cloud droplets would decrease ozone production in high-NO_x environments and enhance ozone destruction in low-NO_x environments (Lelieveld and Crutzen, 1990). Computational simulations suggest that ozone
490 could be stabilized within the air-water interface (within the first 4 Å), and that modification of the ozone UV-vis absorption cross section and activation of photolytic pathways at the interface can increase the ozone photolysis rate constant by more than a factor of 20 (Anglada et al., 2014). The observations from the RF03-C legs may represent the first field evidence of these proposed processes. Critically, the RF03-C-1 flux leg performed at 107 m immediately prior to
495 the RF03-C-2 887 m leg found fluxes below detection for all three ozone instruments. Thus, if cloud effects are operative, they may well be invisible to surface-based platforms such as ships.

Compared to shipborne measurements taken over the course of days or weeks, the flux legs here are necessarily shorter, with the longest leg being ten minutes and the legs being only ~5 minutes long on average. To assess the consistency between sensors on shorter time scales, the ozone EC
500 fluxes were also calculated in 75-second long quarters for the flux example RF06-A-1 shown in Figure 7. The ozone flux observed in this leg is carried in the first, third, and last quarters, with flux in the second quarter below detection. However, the water vapor flux is above detection in all segments and exhibits different trends from the ozone flux. Since the water vapor and ozone are both carried by the same eddies, the difference in behavior cannot be attributed to
505 meteorology. Rather, the ozone flux variability must reflect true heterogeneity in the ocean and/or atmospheric chemical states. Assuming chemical measurements are available on similar time scales, the ozone flux can help characterize atmospheric chemistry on ~10 km spatial scales. For measuring average fluxes, we recommend flying multiple flux legs over regions of interest for better statistics as ozone fluxes are often near the LOD.

510 4. Conclusions and Outlook

In the aggregate, Fast O₃ and FAIRO instruments operate at comparable frequencies (10 vs 12.5 Hz data rate; 3 Hz practical resolution estimated from the mixing time of zero-air puffs at the Fast O₃ inlet), are accurate within 2%, and have similar LOD at their typical sampling rates (1.5 ppbv). Large excursions in measured ozone vmrs (of up to 30%, or 5 ppbv difference) are
515 sometimes observed in the ratio of high-rate data between the instruments, but the excursions show no systematic behavior with respect to ozone concentration, water vapor or NO_x. These differences did not occur during the flux legs. From an operational standpoint, the FAIRO design is advantageous, because the instrument and pump fit into a single 19" rack and requires no hazardous NO gas.

520 Simultaneous, high-frequency H₂O measurements in the free stream are essential for synchronizing the O₃ sensors and wind measurements and provide context to the interpretation of O₃ EC fluxes. Inlet line delays, clock drifts, and small inaccuracies in clock synchronizations lead to time offsets that are difficult to characterize with certainty. Correlation events between water vapor and ozone present direct means for clock synchronization. In principle, an ozone
525 time lag could be prescribed by matching the ozone time stamp to the water vapor time stamp and searching for time lag at which water vapor flux peaks since the water vapor flux is always above detection. In practice, clock drifts still necessitate a search for a cross-covariance peak in the ozone flux, albeit in a constrained time window.

The availability of three ozone instruments during TI³GER allowed for the estimation of the
530 "true" LOD of the ozone flux (LOD_{ECflux}) using the standard deviation of the EC fluxes measured by each instrument. We use this information to provide a modified procedure to

estimate error and LOD_{ECflux} : the RE_{RMSE} formula (eq. 7) (Langford et al. 2015) is combined with the concept of “integral time scale” (Lenschow et al., 2000). We find that the “true” LOD_{ECflux} (defined as the 95% CI on the mean EC flux) is overestimated by the EC flux uncertainty on an individual sensor when Γ is a large time window (30 sec, as used in Lenschow et al.). Estimating the RE_{RMSE} over a smaller time window shrinks the RM_{RMSE} , and brings the EC flux uncertainty closer to the “true” error inferred from the EC flux standard deviation of three separate sensors, without underestimating the EC flux error. We find that the integral time scale Γ suitable to estimate error is usually a few seconds, and define it here as Γ found by integrating outward from a candidate covariance peak until the first zero-crossing of the covariance integral. Typical LODs for O_3 exchange velocities are 30-50% lower with shorter Γ , with typical $LOD \sim 0.005 \text{ cm s}^{-1}$, limited by spurious covariance peaks that are clearly non-physical as they exceed the believable bounds of instrument synchronization.

Ozone EC fluxes measured from aircraft in the remote MBL can exhibit significant time variability on the order of minutes (6-10 km). A similar variability is not seen in the H_2O EC fluxes. While the H_2O EC fluxes are spatially more homogeneous, and de-facto constant (within 25%), a variability in the O_3 EC fluxes of larger than 600% is observed and highly significant (above $6\text{-}\sigma$ to below detection) on spatial scales of 20 km. This variability is seen consistently by all three sensors over the open ocean environments probed here. Cloud cover can reverse the direction of the O_3 and H_2O fluxes, indicating a source of water vapor and a sink for O_3 above the aircraft, consistent with webcam images of clouds. The drivers of the horizontal variability in O_3 EC fluxes directed into the ocean on fine spatial scales is currently not well understood, but could relate to changes in overhead cloud cover, as well as possibly variability in ocean and

atmospheric states. Future studies are needed, and would benefit from repeat legs and
555 measurements of ocean state variables.

Code Availability

The MATLAB flux toolbox is available at: <https://github.com/AirChem/FluxToolbox>.

Data Availability

All data used in this paper can be found on the TI3GER field catalog, which is available at the
560 following URL: https://www.eol.ucar.edu/field_projects/ti3ger.

Author Contributions

RV designed the TI³GER project, and as mission scientist planned and led research flights. RC
performed data analysis of the EC fluxes and instrument intercomparison, assisted with
instrument calibrations and uninstallation, and led the manuscript preparation. FO and AZ
565 calibrated and deployed the FAIRO instruments and provided the FAIRO data. AF and TC
calibrated and deployed the Fast O₃ instrument and provided Fast O₃ data. AR and CW
calibrated the wind measurements and provided GV data. RC and RV wrote the manuscript, with
contributions from all co-authors.

Competing Interests

570 At least one of the (co-)authors is a member of the editorial board of Atmospheric Measurement
Techniques.

Acknowledgements

Financial support for TI³GER from US National Science Foundation award AGS-2027252 (PI: R. Volkamer) is gratefully acknowledged. RC and RV thank Glenn Wolfe, Erin Delaria and
575 Reem Hannun, and Dongwook Kim for helpful discussions. TI³GER was supported by the National Center for Atmospheric Research, which is a major facility sponsored by the NSF under Cooperative Agreement no. 1852977. The data were collected using NSF's Lower Atmosphere Observing Facilities, which are managed and operated by NCAR's Earth Observing Laboratory. The GV aircraft was operated by the National Center for Atmospheric Research (NCAR) Earth
580 Observing Laboratory's (EOL) Research Aviation Facility (RAF). The NCAR ozone measurements were funded by NSF Lower Atmosphere Observing Facilities and NSF NCAR/Facilities programs.

References

- 585 Altimir, N., Kolari, P., Tuovinen, J.-P., Vesala, T., Bäck, J., Suni, T., Kulmala, M., and Hari, P.: Foliage surface ozone deposition: a role for surface moisture?, *Biogeosciences*, 3, 209–228, <https://doi.org/10.5194/BG-3-209-2006>, 2006.
- 590 Anglada, J. M., Martins-Costa, M., Ruiz-López, M. F., and Francisco, J. S.: Spectroscopic signatures of ozone at the air-water interface and photochemistry implications, *Proc Natl Acad Sci U S A*, 111, 11618–11623, <https://doi.org/10.1073/pnas.1411727111>, 2014.
- Bariteau, L., Helmig, D., Fairall, C. W., Hare, J. E., Hueber, J., and Lang, E. K.: Determination of oceanic ozone deposition by ship-borne eddy covariance flux measurements, *Atmos Meas Tech*, 3, 441–455, <https://doi.org/10.5194/amt-3-441-2010>, 2010.
- 595 Barnes, J. and Mauersberger, K.: Temperature dependence of the ozone absorption cross section at the 253.7-nm mercury line, *Journal of Geophysical Research: Atmospheres*, 92, 14861–14864, <https://doi.org/10.1029/JD092ID12P14861>, 1987.
- 600 Barten, J. G. M., Ganzeveld, L. N., Steeneveld, G. J., Blomquist, B. W., Angot, H., Archer, S. D., Bariteau, L., Beck, I., Boyer, M., von der Gathen, P., Helmig, D., Howard, D., Hueber, J., Jacobi, H. W., Jokinen, T., Laurila, T., Posman, K. M., Quéléver, L., Schmale, J., Shupe, M.

- D., and Krol, M. C.: Low ozone dry deposition rates to sea ice during the MOSAiC field campaign: Implications for the Arctic boundary layer ozone budget, *Elementa*, 11, <https://doi.org/10.1525/ELEMENTA.2022.00086/195276>, 2023.
- 605 Bauer, M. R., Hultman, N. E., Panek, J. A., and Goldstein, A. H.: Ozone deposition to a ponderosa pine plantation in the Sierra Nevada Mountains (CA): A comparison of two different climatic years, *Journal of Geophysical Research: Atmospheres*, 105, 22123–22136, <https://doi.org/10.1029/2000JD900168>, 2000.
- 610 Boylan, P., Helmig, D., and Park, J. H.: Characterization and mitigation of water vapor effects in the measurement of ozone by chemiluminescence with nitric oxide, *Atmos Meas Tech*, 7, 1231–1244, <https://doi.org/10.5194/AMT-7-1231-2014>, 2014.
- Chiu, R., Tinel, L., Gonzalez, L., Ciuraru, R., Bernard, F., George, C., and Volkamer, R.: UV photochemistry of carboxylic acids at the air-sea boundary: A relevant source of glyoxal and other oxygenated VOC in the marine atmosphere, *Geophys Res Lett*, 44, 1079–1087, <https://doi.org/10.1002/2016GL071240>, 2017.
- 615 Clifton, O. E., Fiore, A. M., Massman, W. J., Baublitz, C. B., Coyle, M., Emberson, L., Fares, S., Farmer, D. K., Gentine, P., Gerosa, G., Guenther, A. B., Helmig, D., Lombardozzi, D. L., Munger, J. W., Patton, E. G., Pusede, S. E., Schwede, D. B., Silva, S. J., Sörgel, M., Steiner, A. L., and Tai, A. P. K.: Dry Deposition of Ozone Over Land: Processes, Measurement, and Modeling, *Reviews of Geophysics*, 58, e2019RG000670, <https://doi.org/10.1029/2019RG000670>, 2020.
- 620 Conley, S. A., Faloon, I. C., Lenschow, D. H., Campos, T., Heizer, C., Weinheimer, A., Cantrell, C. A., Mauldin, R. L., Hornbrook, R. S., Pollack, I., and Bandy, A.: A complete dynamical ozone budget measured in the tropical marine boundary layer during PASE, *J Atmos Chem*, 68, 55–70, <https://doi.org/10.1007/s10874-011-9195-0>, 2011.
- 625 Deardorff, J. W.: On the entrainment rate of a stratocumulus-topped mixed layer, *Quarterly Journal of the Royal Meteorological Society*, 102, 563–582, <https://doi.org/10.1002/QJ.49710243306>, 1976.
- 630 Dunlea, E. J., Herndon, S. C., Nelson, D. D., Volkamer, R. M., Lamb, B. K., Allwine, E. J., Grutter, M., Ramos Villegas, C. R., Marquez, C., Blanco, S., Cardenas, B., Kolb, C. E., Molina, L. T., and Molina, M. J.: Technical note: Evaluation of standard ultraviolet absorption ozone monitors in a polluted urban environment, *Atmos. Chem. Phys*, 6, 3163–3180, 2006.
- 635 El-Madany, T. S., Niklasch, K., and Klemm, O.: Stomatal and Non-Stomatal Turbulent Deposition Flux of Ozone to a Managed Peatland, *Atmosphere 2017*, Vol. 8, Page 175, 8, 175, <https://doi.org/10.3390/ATMOS8090175>, 2017.
- Ermel, M., Oswald, R., Mayer, J. C., Moravek, A., Song, G., Beck, M., Meixner, F. X., and Trebs, I.: Preparation methods to optimize the performance of sensor discs for fast

chemiluminescence ozone analyzers, *Environ Sci Technol*, 47, 1930–1936,
https://doi.org/10.1021/ES3040363/SUPPL_FILE/ES3040363_SI_001.PDF, 2013.

- 640 Faloona, I., Lenschow, D. H., Campos, T., Stevens, B., van Zanten, M., Blomquist, B., Thornton, D., Bandy, A., and Gerber, H.: Observations of Entrainment in Eastern Pacific Marine Stratocumulus Using Three Conserved Scalars, *J Atmos Sci*, 62, 3268–3285,
<https://doi.org/10.1175/JAS3541.1>, 2005.
- 645 Fares, S., Savi, F., Muller, J., Matteucci, G., and Paoletti, E.: Simultaneous measurements of above and below canopy ozone fluxes help partitioning ozone deposition between its various sinks in a Mediterranean Oak Forest, *Agric For Meteorol*, 198–199, 181–191,
<https://doi.org/10.1016/J.AGRFORMET.2014.08.014>, 2014.
- 650 Finco, A., Marzuoli, R., Chiesa, M., and Gerosa, G.: Ozone risk assessment for an Alpine larch forest in two vegetative seasons with different approaches: comparison of POD1 and AOT40, *Environmental Science and Pollution Research*, 24, 26238–26248,
<https://doi.org/10.1007/S11356-017-9301-1/FIGURES/6>, 2017.
- Gallagher, M. W., Beswick, K. M., and Coe, H.: Ozone deposition to coastal waters, *Quarterly Journal of the Royal Meteorological Society*, 127, 539–558,
<https://doi.org/10.1002/QJ.49712757215>, 2001.
- 655 Ganzeveld, L., Helmig, D., Fairall, C. W., Hare, J., and Pozzer, A.: Atmosphere-ocean ozone exchange: A global modeling study of biogeochemical, atmospheric, and waterside turbulence dependencies, *Global Biogeochem. Cycles*, 23, 4021,
<https://doi.org/10.1029/2008GB003301>, 2009.
- 660 Güsten, H. and Heinrich, G.: On-line measurements of ozone surface fluxes: Part I. Methodology and instrumentation, *Atmos Environ*, 30, 897–909, [https://doi.org/10.1016/1352-2310\(95\)00269-3](https://doi.org/10.1016/1352-2310(95)00269-3), 1996.
- Güsten, H., Heinrich, G., Schmidt, R. W. H., and Schurath, U.: A novel ozone sensor for direct eddy flux measurements, *J Atmos Chem*, 14, 73–84,
<https://doi.org/10.1007/BF00115224/METRICS>, 1992.
- 665 Güsten, H., Heinrich, G., Mönnich, E., Sprung, D., Weppner, J., Ramadan, A. B., Ezz El-Din, M. R. M., Ahmed, D. M., and Hassan, G. K. Y.: On-line measurements of ozone surface fluxes: Part II. Surface-level ozone fluxes onto the Sahara desert, *Atmos Environ*, 30, 911–918, [https://doi.org/10.1016/1352-2310\(95\)00270-7](https://doi.org/10.1016/1352-2310(95)00270-7), 1996.
- 670 Hannun, R. A., Swanson, A. K., Bailey, S. A., Hanisco, T. F., Paul Bui, T., Bourgeois, I., Peischl, J., and Ryerson, T. B.: A cavity-enhanced ultraviolet absorption instrument for high-precision, fast-Time-response ozone measurements, *Atmos Meas Tech*, 13, 6877–6887,
<https://doi.org/10.5194/AMT-13-6877-2020>, 2020.
- Helmig, D., Lang, E. K., Bariteau, L., Boylan, P., Fairall, C. W., Ganzeveld, L., Hare, J. E., Hueber, J., and Pallandt, M.: Atmosphere-ocean ozone fluxes during the TexAQS 2006,

- 675 STRATUS 2006, GOMECC 2007, GasEx 2008, and AMMA 2008 cruises, *Journal of Geophysical Research: Atmospheres*, 117, <https://doi.org/10.1029/2011JD015955>, 2006.
- Juráň, S., Šigut, L., Holub, P., Fares, S., Klem, K., Grace, J., and Urban, O.: Ozone flux and ozone deposition in a mountain spruce forest are modulated by sky conditions, *Science of The Total Environment*, 672, 296–304, <https://doi.org/10.1016/J.SCITOTENV.2019.03.491>, 2019.
- 680 Kammer, J., Lamaud, E., Bonnefond, J. M., Garrigou, D., Flaud, P. M., Perraudin, E., and Villenave, E.: Ozone production in a maritime pine forest in water-stressed conditions, *Atmos Environ*, 197, 131–140, <https://doi.org/10.1016/J.ATMOSENV.2018.10.021>, 2019.
- Lamaud, E., Carrara, A., Brunet, Y., Lopez, A., and Druilhet, A.: Ozone fluxes above and within a pine forest canopy in dry and wet conditions, *Atmos Environ*, 36, 77–88, [https://doi.org/10.1016/S1352-2310\(01\)00468-X](https://doi.org/10.1016/S1352-2310(01)00468-X), 2002.
- 685 Lamaud, E., Loubet, B., Irvine, M., Stella, P., Personne, E., and Cellier, P.: Partitioning of ozone deposition over a developed maize crop between stomatal and non-stomatal uptakes, using eddy-covariance flux measurements and modelling, *Agric For Meteorol*, 149, 1385–1396, <https://doi.org/10.1016/J.AGRFORMET.2009.03.017>, 2009.
- 690 Langford, B., Acton, W., Ammann, C., Valach, A., and Nemitz, E.: Eddy-covariance data with low signal-to-noise ratio: Time-lag determination, uncertainties and limit of detection, *Atmos Meas Tech*, 8, 4197–4213, <https://doi.org/10.5194/AMT-8-4197-2015>, 2015.
- Relievel, J. and Crutzen, P. J.: Influences of cloud photochemical processes on tropospheric ozone, *Nature*, 343, 227–233, <https://doi.org/10.1038/343227a0>, 1990.
- 695 Lenschow, D. H. and Raupach, M. R.: The attenuation of fluctuations in scalar concentrations through sampling tubes, *J Geophys Res*, 96, 15259–15268, <https://doi.org/10.1029/91JD01437>, 1991.
- Lenschow, D. H., Delany, A. C., Stankov, B. B., and Stedman, D. H.: Airborne measurements of the vertical flux of ozone in the boundary layer, *Boundary Layer Meteorol*, 19, 249–265, <https://doi.org/10.1007/BF00117223>/METRICS, 1980.
- 700 Lenschow, D. H., Wulfmeyer, V., and Senff, C.: Measuring Second-through Fourth-Order Moments in Noisy Data, *J Atmos Ocean Technol*, 17, 1330–1347, [https://doi.org/https://doi.org/10.1175/1520-0426\(2000\)017<1330:MSTFOM>2.0.CO;2](https://doi.org/https://doi.org/10.1175/1520-0426(2000)017<1330:MSTFOM>2.0.CO;2), 2000.
- 705 Loubet, B., Cellier, P., Fléchar, C., Zurfluh, O., Irvine, M., Lamaud, E., Stella, P., Roche, R., Durand, B., Flura, D., Masson, S., Laville, P., Garrigou, D., Personne, E., Chelle, M., and Castell, J. F.: Investigating discrepancies in heat, CO₂ fluxes and O₃ deposition velocity over maize as measured by the eddy-covariance and the aerodynamic gradient methods, *Agric For Meteorol*, 169, 35–50, <https://doi.org/10.1016/J.AGRFORMET.2012.09.010>, 2013.
- 710

- Massman, W. J., Macpherson, J. I., Delany, A., Den Hartog, G., Neumann, H. H., Oncley, S. P., Pearson, R., Pederson, J., and Shaw, R. H.: Surface conductances for ozone uptake derived from aircraft eddy correlation data, *Atmos Environ*, 29, 3181–3188, [https://doi.org/10.1016/1352-2310\(94\)00330-N](https://doi.org/10.1016/1352-2310(94)00330-N), 1995.
- 715
- Matthews, R. D., Sawyer, R. F., and Schefer, R. W.: Interferences in chemiluminescent measurement of nitric oxide and nitrogen dioxide emissions from combustion systems, *Environ Sci Technol*, 11, 1092–1096, <https://doi.org/10.1021/es60135a005>, 1977.
- Muller, J. B. A., Coyle, M., Fowler, D., Gallagher, M. W., Nemitz, E. G., and Perciva, C. J.: Comparison of ozone fluxes over grassland by gradient and eddy covariance technique, *Atmospheric Science Letters*, 10, 164–169, <https://doi.org/10.1002/ASL.226>, 2009.
- 720
- Muller, J. B. A., Percival, C. J., Gallagher, M. W., Fowler, D., Coyle, M., and Nemitz, E.: Sources of uncertainty in eddy covariance ozone flux measurements made by dry chemiluminescence fast response analysers, *Atmos Meas Tech*, 3, 163–176, <https://doi.org/10.5194/AMT-3-163-2010>, 2010.
- 725
- Muller, J. B. A., Dorsey, J. R., Flynn, M., Gallagher, M. W., Percival, C. J., Shallcross, D. E., Archibald, A., Roscoe, H. K., Obbard, R. W., Atkinson, H. M., Lee, J. D., Moller, S. J., and Carpenter, L. J.: Energy and ozone fluxes over sea ice, *Atmos Environ*, 47, 218–225, <https://doi.org/10.1016/J.ATMOSENV.2011.11.013>, 2012.
- 730
- Pearson, R., Jr. and Stedman, D.: Instrumentation for fast-response ozone measurements from aircraft, *Atmos. Technol.*, 12, 51–54, 1980.
- Plake, D., Stella, P., Moravek, A., Mayer, J. C., Ammann, C., Held, A., and Trebs, I.: Comparison of ozone deposition measured with the dynamic chamber and the eddy covariance method, *Agric For Meteorol*, 206, 97–112, <https://doi.org/10.1016/J.AGRFORMET.2015.02.014>, 2015.
- 735
- Rannik, Ü., Altimir, N., Mammarella, I., Bäck, J., Rinne, J., Ruuskanen, T. M., Hari, P., Vesala, T., and Kulmala, M.: Ozone deposition into a boreal forest over a decade of observations: Evaluating deposition partitioning and driving variables, *Atmos Chem Phys*, 12, 12165–12182, <https://doi.org/10.5194/ACP-12-12165-2012>, 2012.
- 740
- Ridley, B. A. and Howlett, L. C.: An instrument for nitric oxide measurements in the stratosphere, *Review of Scientific Instruments*, 45, 742–746, <https://doi.org/10.1063/1.1686726>, 1974.
- Ridley, B. A., Schiff, H. I., and Welge, K. H.: Measurement of NO in the Stratosphere by NO/O₃ Chemiluminescence (COM-72-10476), 1972.
- 745
- Ridley, B. A., Grahek, F. E., and Walega, J. G.: A Small High-Sensitivity, Medium-Response Ozone Detector Suitable for Measurements from Light Aircraft, *J Atmos Ocean Technol*, 9, 142–148, [https://doi.org/10.1175/1520-0426\(1992\)009%3C0142:ASHSMR%3E2.0.CO;2](https://doi.org/10.1175/1520-0426(1992)009%3C0142:ASHSMR%3E2.0.CO;2), 1992.

- 750 Rolph, G., Stein, A., and Stunder, B.: Real-time Environmental Applications and Display
sYstem: READY, *Environmental Modelling & Software*, 95, 210–228,
<https://doi.org/10.1016/J.ENVSOF.2017.06.025>, 2017.
- Saiz-Lopez, A., Plane, J. M. C. C., Baker, A. R., Carpenter, L. J., von Glasow, R., Gómez Martín,
J. C., McFiggans, G., and Saunders, R. W.: Atmospheric Chemistry of Iodine, *Chem Rev*,
112, 1773–1804, <https://doi.org/10.1021/cr200029u>, 2012.
- 755 Schurath, U., Speuser, W., and Schmidt, R.: Principle and application of a fast sensor for
atmospheric ozone, *Fresenius J Anal Chem*, 340, 544–547,
<https://doi.org/10.1007/BF00322426>/METRICS, 1991.
- Stein, A. F., Draxler, R. R., Rolph, G. D., Stunder, B. J. B., Cohen, M. D., and Ngan, F.: NOAA’s
HYSPLIT Atmospheric Transport and Dispersion Modeling System, *Bull Am Meteorol*
760 *Soc*, 96, 2059–2077, <https://doi.org/10.1175/BAMS-D-14-00110.1>, 2015.
- Stella, P., Loubet, B., Lamaud, E., Laville, P., and Cellier, P.: Ozone deposition onto bare soil: A
new parameterisation, *Agric For Meteorol*, 151, 669–681,
<https://doi.org/10.1016/J.AGRFORMET.2011.01.015>, 2011.
- Torrence, C. and Compo, G. P.: A Practical Guide to Wavelet Analysis, *Bull Am Meteorol Soc*,
765 79, 61–78, [https://doi.org/10.1175/1520-0477\(1998\)079<0061:APGTWA>2.0.CO;2](https://doi.org/10.1175/1520-0477(1998)079<0061:APGTWA>2.0.CO;2), 1998.
- Vermeuel, M. P., Cleary, P. A., Desai, A. R., and Bertram, T. H.: Simultaneous Measurements of
O₃ and HCOOH Vertical Fluxes Indicate Rapid In-Canopy Terpene Chemistry Enhances
O₃ Removal Over Mixed Temperate Forests, *Geophys Res Lett*, 48, e2020GL090996,
<https://doi.org/10.1029/2020GL090996>, 2021.
- 770 Wohlfahrt, G., Hörtnagl, L., Hammerle, A., Graus, M., and Hansel, A.: Measuring eddy
covariance fluxes of ozone with a slow-response analyser, *Atmos Environ*, 43, 4570–4576,
<https://doi.org/10.1016/J.ATMOSENV.2009.06.031>, 2009.
- Wolfe, G. M.: AirChem/FluxToolbox: Collections of scripts for eddy covariance flux
calculations (both traditional and wavelet-based).:
775 <https://github.com/AirChem/FluxToolbox>, last access: 18 May 2023.
- Wolfe, G. M., Hanisco, T. F., Arkinson, H. L., Bui, T. P., Crounse, J. D., Dean-Day, J., Goldstein,
A., Guenther, A., Hall, S. R., Huey, G., Jacob, D. J., Karl, T., Kim, P. S., Liu, X., Marvin,
M. R., Mikoviny, T., Misztal, P. K., Nguyen, T. B., Peischl, J., Pollack, I., Ryerson, T., St.
Clair, J. M., Teng, A., Travis, K. R., Ullmann, K., Wennberg, P. O., and Wisthaler, A.:
780 Quantifying sources and sinks of reactive gases in the lower atmosphere using airborne flux
observations, *Geophys Res Lett*, 42, 8231–8240, <https://doi.org/10.1002/2015GL065839>,
2015.
- Wolfe, G. M., Kawa, S. R., Hanisco, T. F., Hannun, R. A., Newman, P. A., Swanson, A., Bailey,
S., Barrick, J., Thornhill, K. L., Diskin, G., DiGangi, J., Nowak, J. B., Sorenson, C., Bland,
785 G., Yungel, J. K., and Swenson, C. A.: The NASA Carbon Airborne Flux Experiment

(CARAFE): Instrumentation and methodology, *Atmos Meas Tech*, 11, 1757–1776, <https://doi.org/10.5194/amt-11-1757-2018>, 2018.

790 Zahn, A., Weppner, J., Widmann, H., Schlote-Holubek, K., Burger, B., Köhler, T., and Franke, H.: A fast and precise chemiluminescence ozone detector for eddy flux and airborne application, *Atmos. Meas. Tech*, 5, 363–375, <https://doi.org/10.5194/amt-5-363-2012>, 2012.

Zeller, K.: Summer and autumn ozone fluxes to a forest in the Czech Republic Brdy Mountains, *Environmental Pollution*, 119, 269–278, [https://doi.org/10.1016/S0269-7491\(01\)00176-2](https://doi.org/10.1016/S0269-7491(01)00176-2), 2002.

795 Zeller, K. F. and Nikolov, N. T.: Quantifying simultaneous fluxes of ozone, carbon dioxide and water vapor above a subalpine forest ecosystem, *Environmental Pollution*, 107, 1–20, [https://doi.org/10.1016/S0269-7491\(99\)00156-6](https://doi.org/10.1016/S0269-7491(99)00156-6), 2000.

800 Zhu, Z., Zhao, F., Voss, L., Xu, L., Sun, X., Yu, G., and Meixner, F. X.: The effects of different calibration and frequency response correction methods on eddy covariance ozone flux measured with a dry chemiluminescence analyzer, *Agric For Meteorol*, 213, 114–125, <https://doi.org/10.1016/J.AGRFORMET.2015.06.016>, 2015.

Zhu, Z., Tang, X., and Zhao, F.: Comparison of Ozone Fluxes over a Maize Field Measured with Gradient Methods and the Eddy Covariance Technique, *Adv Atmos Sci*, 37, 586–596, <https://doi.org/https://doi.org/10.1007/s00376-020-9217-4>, 2020.

805 Zhu, Z. L., Sun, X. M., Dong, Y. S., Zhao, F. H., and Meixner, F. X.: Diurnal variation of ozone flux over corn field in Northwestern Shandong Plain of China, *Sci China Earth Sci*, 57, 503–511, <https://doi.org/10.1007/S11430-013-4797-9/METRICS>, 2014.

810 Zondlo, M. A., Paige, M. E., Massick, S. M., and Silver, J. A.: Vertical cavity laser hygrometer for the National Science Foundation Gulfstream-V aircraft, *Journal of Geophysical Research Atmospheres*, 115, <https://doi.org/10.1029/2010JD014445>, 2010.

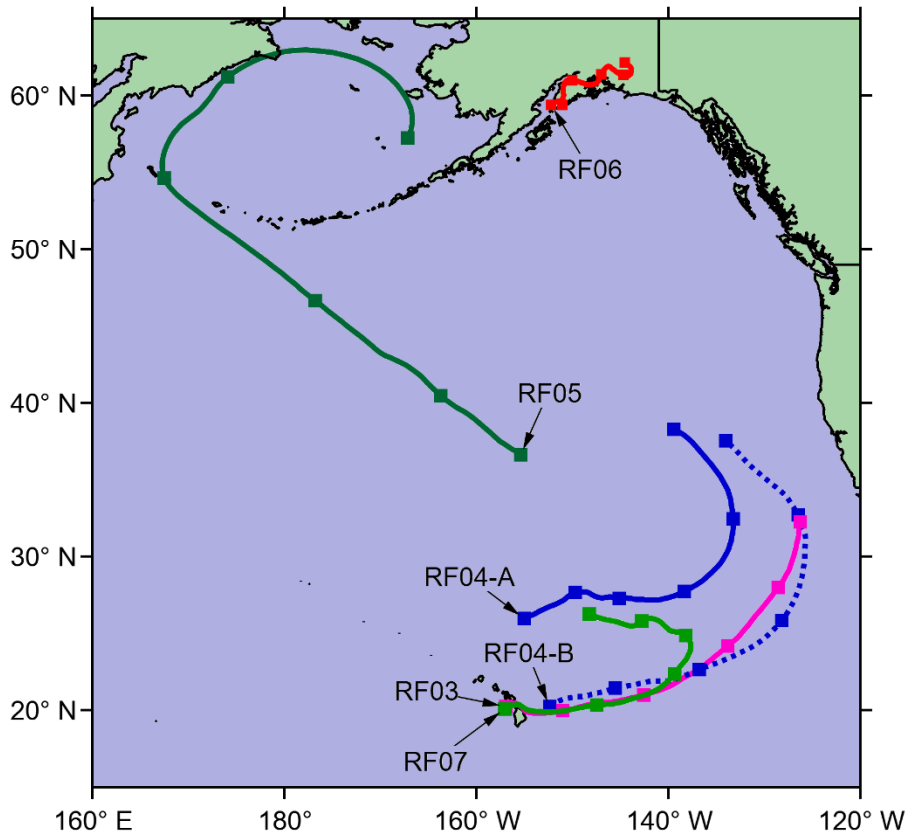
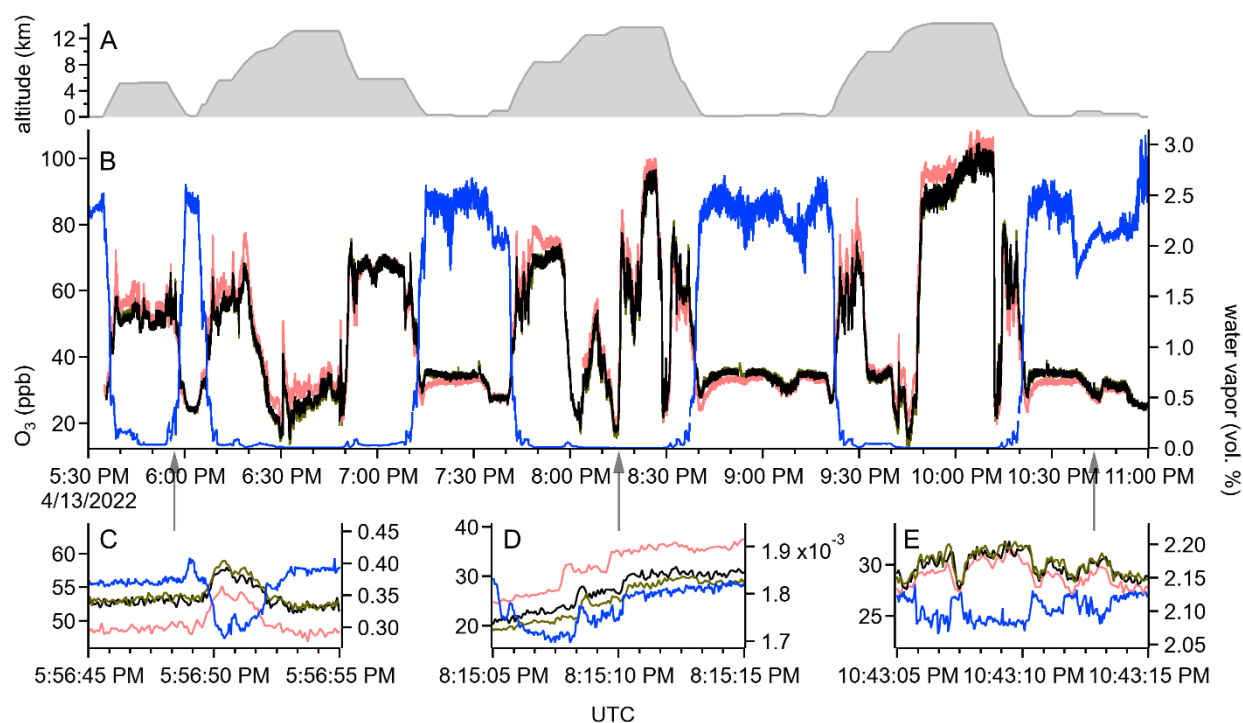


Figure 1. Map of flux legs and back-trajectories during TI³GER. Square markers indicate 24-hour periods, and the arrows mark the location of the flux legs.



815

Figure 2. Time stamp synchronization based on the H₂O and O₃ time series. VCSEL data are shown in blue, Fast O₃ data in salmon, FAIRO 1 in black, and FAIRO 2 in dark olive. All traces are shown at the native instrument resolution (25 Hz for VCSEL, 12.5 Hz for the FAIROs, and 10 Hz for Fast O₃). A: altitude time series. B: time series for the entire flight. C-E: Zooms to cross-covariance events with gray arrows pointing to exact times.

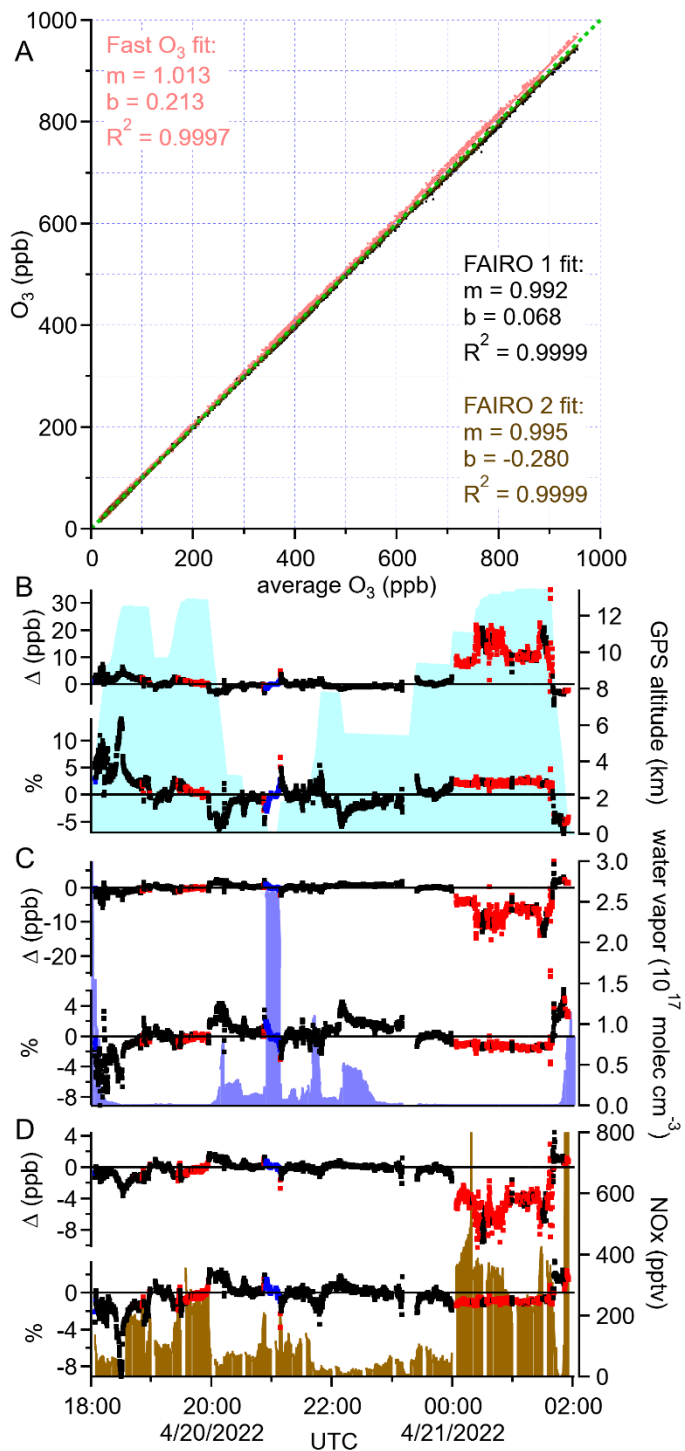
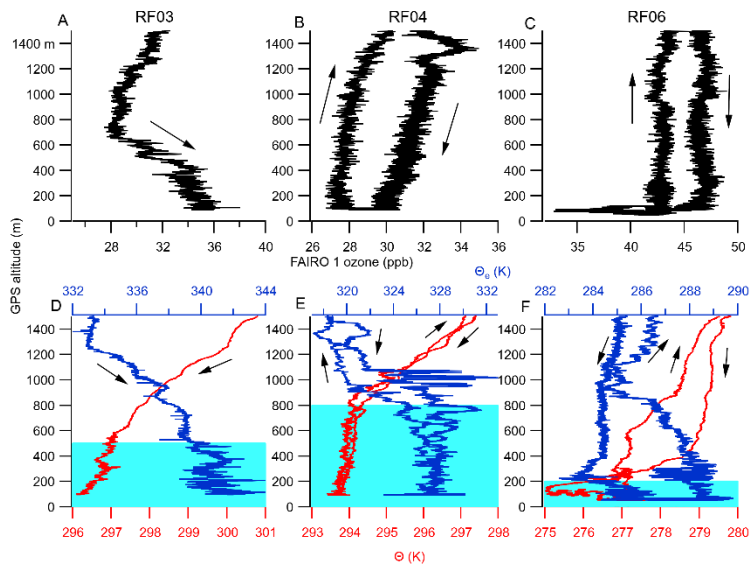
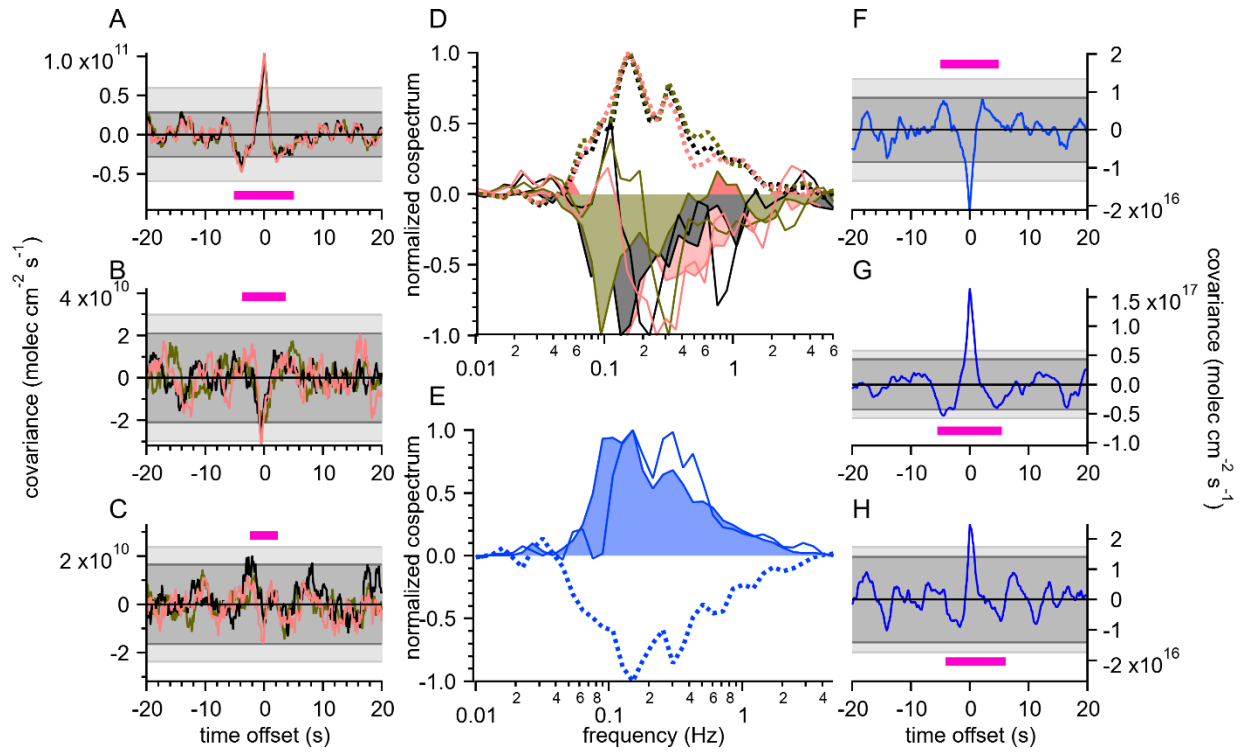


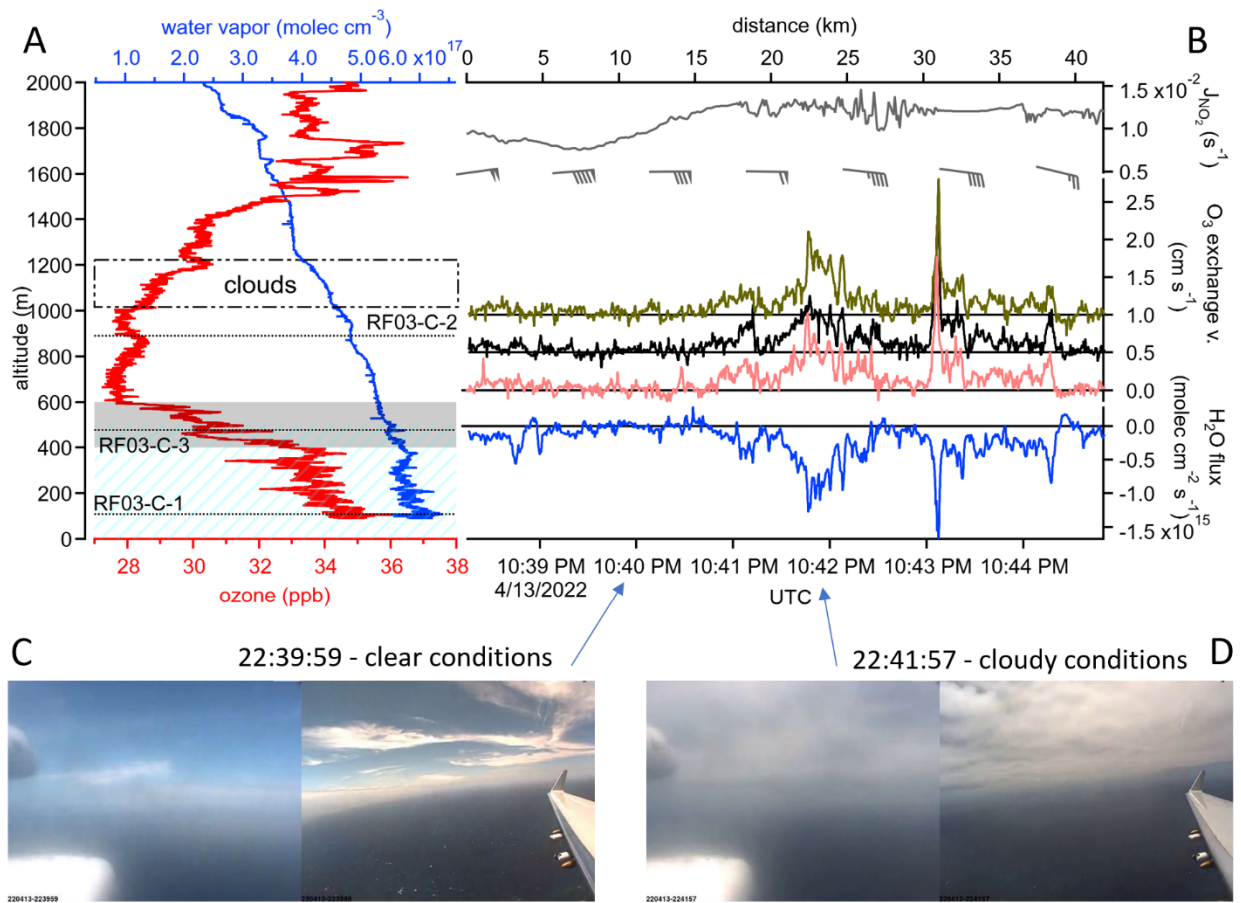
Figure 3. A: Aggregated data from RF03-07 with fits relative to global average; one-to-one line in green. Absolute and relative differences from average during RF05 for Fast O₃ in Panel B; FAIRO 1 in Panel C; and FAIRO 2 in Panel D. Background shading for GPS altitude in Panel B, VCSEL in Panel C, and NO_x in Panel D.



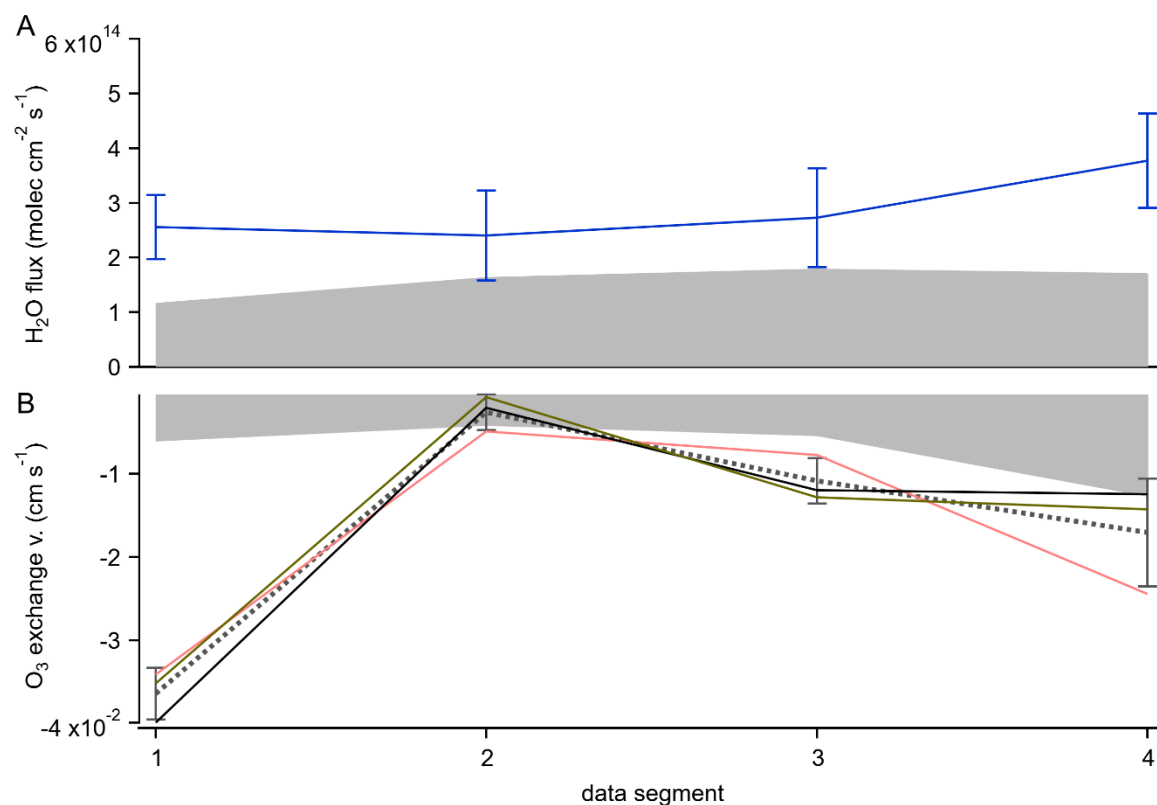
825 Figure 4. A-C: Profiles of ozone during RF03-C, RF04-A, and RF06-A, respectively. D-F: Corresponding potential temperature and equivalent potential temperature profiles for RF03-C, RF04-A, and RF06-A, respectively. MBL height is shown as light blue shading. Arrows indicate profile ascents and descents.



830 Figure 5. Cross-covariance plots for RF03-C-2 (A), RF04-A-1 (B), and RF06-A-1 (C), and their respective water vapor fluxes (F-H). Normalized cospectra are shown in D and E. Detrending the data at 10 s removes spectral power and frequencies below 0.1 Hz. For ozone data, Fast O₃ is shown in salmon, FAIRO 1 in black, and FAIRO 2 in olive. In Panels D and E, RF03 is shown as a dotted line, RF04 as a shade to zero, and RF06 as a solid line. Integral time scales are shown as fuchsia bars.



835 Figure 6. Ozone and water vapor vertical profiles and time series for EC fluxes from the RF03-C leg. Ozone profile
 is the average of all three instruments. Dashed lines indicate flight altitudes; dashed rectangle represents visually
 840 estimated cloud layer. Right: J_{NO_2} in gray, fluxes from Fast O₃ (salmon), FAIRO 1 (black), FAIRO 2 (olive), and
 VCSEL (blue). Vertical offsets of 0.5 cm s^{-1} and 1 cm s^{-1} have been added to FAIRO 1 and 2 to better illustrate the
 close agreement between the three O₃ instruments. Images of the webcams from RF03 flight movies illustrate cloud
 cover conditions.



845 Figure 7. Segments of RF06-A-1. Panel A: VCSEL is shown in blue. Error bars represent modified Langford RE_{RMSE}. Panel B: FO3 in salmon, FAIRO 1 in black, and FAIRO 2 in dark olive. The average is shown as the dotted line. Error bars represent standard deviation. In both panels, the 95% LOD is shaded. Each data segment is 75 seconds long.

flight	average (ppb)	max (ppb)	FO3 slope	FO3 offset (ppb)	F1 slope	F1 offset (ppb)	F2 slope	F2 offset (ppb)
RF03	47.4	103	1.028	0.44	0.982	0.02	0.990	-0.46
RF04	76.5	409	1.029	-0.03	0.981	0.24	0.989	-0.21
RF05	172.8	955	1.024	-1.40	0.985	1.10	0.991	0.34
RF06	223.0	887	1.000	0.15	0.998	0.15	0.998	-0.30
RF07	78.6	177	1.014	0.08	0.992	-0.04	0.994	-0.04

Table 1. Linear fit parameters of individual instruments to average.

exchange velocity (cm s^{-1})

Leg Code	Date UTC	Start UTC	End UTC	location	alt (m)	Fast O3	FAIRO 1	FAIRO 2	average	st. dev.
RF03-A-1	4/13/2022	19:16:43	19:20:13	off SW coast of HI	312	+0.037	+0.020	+0.015	+0.024	0.012
RF03-B-1	4/13/2022	20:45:33	20:52:08	off SW coast of HI	101	+0.033	+0.014	+0.003	+0.017	0.015
RF03-C-2	4/13/2022	22:38:15	22:44:51	off SW coast of HI	889	+0.131	+0.135	+0.136	+0.134	0.003
RF03-C-3	4/13/2022	22:46:02	22:54:15	off SW coast of HI	476	+0.099	+0.093	+0.100	+0.097	0.004
RF04-A-1	4/15/2022	21:16:20	21:21:46	North of HI	93	-0.042	-0.037	-0.030	-0.036	0.006
RF04-A-2	4/15/2022	21:22:12	21:25:50	North of HI	101	-0.030	-0.014	-0.017	-0.021	0.008
RF06-A-1	4/21/2022	19:39:47	19:44:44	off AK coast	58	-0.015	-0.008	-0.009	-0.010	0.004
RF06-B-1	4/22/2022	02:28:59	02:32:01	halfway between AK and HI	116	+0.022	+0.024	+0.024	+0.023	0.001
RF07-A-1	4/23/2022	21:43:30	21:49:20	west of HI airport	116	-0.017	-0.013	-0.014	-0.015	0.002
RF07-A-3	4/23/2022	22:04:07	22:06:45	west of HI airport	778	-0.012	-0.015	-0.015	-0.014	0.002
RF07-A-4	4/23/2022	22:11:24	22:16:08	west of HI airport	472	-0.035	-0.029	-0.036	-0.033	0.004

Table 2. Summary of ozone EC flux results.